

Research Article

Open Access



# Fabrication of MOF-derived porous Au@Co-ZnO nanostructures with excellent C<sub>2</sub>H<sub>5</sub>OH sensing performance

Kaiwen Tian<sup>1</sup>, Yukang Fu<sup>1</sup>, Inzizamul Haq<sup>1,2</sup>, Shuangyang Kuang<sup>1</sup>, Gaojie Xiong<sup>1</sup>, Zeyuan Zhao<sup>1</sup>, Tianyu Zhou<sup>1</sup>, Jun Weng<sup>1</sup>, Xiang Peng<sup>1</sup>, Liwei Xiong<sup>1</sup>

<sup>1</sup>Hubei Key Laboratory of Plasma Chemistry and Advanced Materials, School of Materials Science and Engineering, Wuhan Institute of Technology, Wuhan 430205, Hubei, China.

<sup>2</sup>Department of Physics, Government Degree College, Swat 18000, KP, Pakistan.

**Correspondence to:** Prof. Shuangyang Kuang and Prof. Liwei Xiong, Hubei Key Laboratory of Plasma Chemistry and Advanced Materials, School of Materials Science and Engineering, Wuhan Institute of Technology, 206 Guanggu 1st Road, Wuhan 430205, Hubei, China. E-mails: 22041201@wit.edu.cn; zhily2000@126.com

**How to cite this article:** Tian, K.; Fu, Y.; Haq, I.; Kuang, S.; Xiong, G.; Zhao, Z.; Zhou, T.; Weng, J.; Peng, X.; Xiong, L. Fabrication of MOF-derived porous Au@Co-ZnO nanostructures with excellent C<sub>2</sub>H<sub>5</sub>OH sensing performance. *Microstructures* 2025, 5, 2025041. <https://dx.doi.org/10.20517/microstructures.2024.110>

**Received:** 1 Nov 2024 **First Decision:** 21 Nov 2024 **Revised:** 9 Dec 2024 **Accepted:** 12 Dec 2024 **Published:** 15 Apr 2025

**Academic Editor:** Zhanxi Fan **Copy Editor:** Shu-Yuan Duan **Production Editor:** Shu-Yuan Duan

## Abstract

**Aim:** Zinc oxide (ZnO) is an n-type semiconductor with a wide bandgap, excellent electron mobility, and stable chemical characteristics, making it potentially applicable in the field of gas sensing. However, conventional ZnO-based gas sensors face challenges such as high operating temperatures and low sensitivity.

**Methods:** In this paper, we first synthesized ZIF-8 with a rhombic dodecahedron structure using a room-temperature chemical precipitation method. By doping ZIF-8 with cobalt (Co) and exchanging gold ions, followed by calcination in air, we obtained a metal-organic framework (MOF) derived porous Au@Co-ZnO nanostructure.

**Results:** This nanostructure retained the large specific surface area and porous characteristics of ZIF-8, while its gas sensing performance was significantly enhanced compared to the pure MOF-derived ZnO nanostructure, due to Co doping and gold nanoparticle modification. At an ethanol concentration of 100 ppm, the Au@Co-ZnO sample demonstrated its best performance at 140 °C, with a response value of 205.3. This result was 28.9 times higher compared to the pure ZnO sample, which showed a response value of 7.1 under identical conditions. Additionally, the optimal operating temperature was 40 °C lower than that of the pure ZnO sample (180 °C). Furthermore, the Au@Co-ZnO samples demonstrated good stability and selectivity for ethanol gas.



© The Author(s) 2025. **Open Access** This article is licensed under a Creative Commons Attribution 4.0 International License (<https://creativecommons.org/licenses/by/4.0/>), which permits unrestricted use, sharing, adaptation, distribution and reproduction in any medium or format, for any purpose, even commercially, as long as you give appropriate credit to the original author(s) and the source, provide a link to the Creative Commons license, and indicate if changes were made.

**Conclusion:** The proposed MOF-derived porous Au@Co-ZnO nanostructures not only advance the application of MOF-derived materials in gas detection but also offer a novel approach for boosting the gas-sensing performance of other metal oxide materials.

**Keywords:** Zinc oxide, ZIF-8, gas sensor, ethanol testing

## INTRODUCTION

Ethanol is a colorless, transparent liquid at room temperature and standard atmospheric pressure, widely used in industrial production, food manufacturing, healthcare, and fuel industries<sup>[1]</sup>. It is highly flammable and volatile, and if undetected leaks occur, they can pose significant risks to surrounding personnel, particularly in the presence of open flames, potentially leading to irreparable damage. Therefore, developing a gas sensor with high response sensitivity, a low detection limit, and rapid response capability for ethanol detection is crucial. Gas sensors are currently categorized based on their working principles, including semiconductor, electrochemical, optical, solid electrolyte, and catalytic combustion sensors<sup>[2-6]</sup>. Among these, semiconductor gas sensors stand out for their compact size, low cost, and high sensitivity, making them ideal for various applications and extensively researched<sup>[7]</sup>. Metal oxide semiconductors, in particular, are commonly used in gas sensors due to their stability, high detection accuracy, and cost-effectiveness. For instance, oxides such as  $\text{In}_2\text{O}_3$ <sup>[8]</sup>,  $\text{Co}_3\text{O}_4$ <sup>[9]</sup>,  $\text{Cu}_2\text{O}$ <sup>[10]</sup>, and  $\text{SnO}_2$ <sup>[11]</sup> have been reported as effective gas-sensing materials. Additionally, zinc oxide (ZnO) shows great promise in gas detection owing to its high electron mobility, diverse morphological control, and excellent thermal stability.

ZnO is a semiconductor with a direct bandgap, characterized by a high exciton binding energy, high electron mobility, and a wide bandgap. Nanostructured ZnO exhibits excellent optical, piezoelectric, and electrochemical properties, making it widely used in the fabrication of various sensors, including photoelectric, pressure, temperature, and gas sensors<sup>[12-15]</sup>. In recent years, ZnO gas sensors derived from metal-organic frameworks (MOFs) have garnered significant attention due to their large specific surface area and abundant channel gaps. A large surface area provides abundant adsorbable sites for target gases, promoting the adsorption and reaction rates, thereby enhancing the material's gas-sensing performance. ZIF-8, a common MOF material created through coordinating zinc ions with the organic ligand 2-methylimidazole, is valued for its large surface area, structural stability, significant porosity, and ease of synthesis. ZIF-8 can be easily oxidized to form ZnO through calcination in air<sup>[16]</sup>. Ren *et al.* obtained porous ZnO nanocubes derived from MOFs by pyrolyzing ZIF-8 at 500 °C, achieving a response value of 51.41 for 1 ppm  $\text{NO}_2$  at 200 °C - a significant improvement compared to similar work<sup>[17]</sup>. In addition, heterogeneous metal element doping and noble metal modification are also effective methods for enhancing the gas-sensing properties of materials. Bulemo successfully synthesized Ga-doped ZnO strip materials that exhibited a specific surface area of up to 68.5  $\text{m}^2/\text{g}$  using the electrospinning method. At a working temperature of 400 °C, the response value was 21 to 20 ppm acetylene gas, and the detection limit reached 0.2 ppm, which is significantly improved compared to pure ZnO materials<sup>[18]</sup>. Dai *et al.* synthesized Au-modified ZnO rod-like nanoflowers, which demonstrated an extremely fast response time (15 s), a high response value (138 for 100 ppm), and a low detection limit (1 ppm) for ethanolamine detection<sup>[19]</sup>. Despite these advancements, current ZnO-based gas sensors still face challenges, including high operating temperatures and room for improvement in sensitivity. Due to multiple oxidation states of cobalt (Co) (including  $\text{Co}^{2+}$  and  $\text{Co}^{3+}$ ), cobalt ions release more electrons than  $\text{Zn}^{2+}$  ions when doped into ZnO. The ionic radius of  $\text{Co}^{2+}$  is similar to that of  $\text{Zn}^{2+}$ , meaning that the lattice distortion caused by the substitution of  $\text{Co}^{2+}$  for  $\text{Zn}^{2+}$  is relatively small<sup>[20]</sup>. Additionally, the work function of the noble metal Au (5.1 eV) is higher than that of ZnO (4.45 eV), which can produce an electron sensitization effect. Au also exhibits a chemical sensitization effect, both of which significantly enhance the gas response of ZnO<sup>[21]</sup>. Therefore, in this study,

the combination of Co doping and Au loading was used to further improve the gas-sensing performance of MOF-derived ZnO nanostructures.

In this study, the MOF-derived Porous Au@Co-ZnO nanostructure was successfully fabricated, retaining the structural characteristics of ZIF-8 with a large specific surface area and high porosity. Additionally, the gas sensing performance was significantly enhanced compared to pure MOF-derived ZnO due to Co doping and gold nanoparticle modification. The Au@Co-ZnO nanostructure was prepared by calcining ZIF-8 in air after Co doping and gold ion exchange. In 100 ppm ethanol gas, the optimal operating temperature for the Au@Co-ZnO sample was 140 °C, which is 40 °C lower than the 180 °C required for the pure ZnO sample. Moreover, at the same operating temperature (140 °C), the Au@Co-ZnO sample exhibited a response value of 205.3, which is 28.9 times higher than the response value of 7.1 from the pure ZnO sample to 100 ppm ethanol. Additionally, the Au@Co-ZnO sample exhibited excellent stability and selectivity for ethanol. These results confirm the effectiveness of combining Co doping with Au nanoparticle modification, providing a promising strategy for enhancing the gas-sensing property of other metal oxide materials and advancing the application of MOF-derived materials in gas detection.

## MATERIALS AND METHODS

### Materials

Zinc nitrate hexahydrate ( $\text{Zn}(\text{NO}_3)_2 \cdot 6\text{H}_2\text{O}$ ,  $\geq 99.0\%$ ), cobalt nitrate hexahydrate ( $\text{Co}(\text{NO}_3)_2 \cdot 6\text{H}_2\text{O}$ ,  $\geq 99.0\%$ ), 2-methylimidazole ( $\text{C}_4\text{H}_6\text{N}_2$ , 98%), methanol ( $\text{CH}_3\text{OH}$ ,  $\geq 99.5\%$ ), and anhydrous ethanol ( $\text{C}_2\text{H}_5\text{OH}$ ,  $\geq 99.7\%$ ) were purchased from Sinopharm Reagent Group. Gold chloride trihydrate ( $\text{HAuCl}_4 \cdot 3\text{H}_2\text{O}$ ,  $\geq 99.9\%$ ) was purchased from Aladdin Chemicals Co., Ltd.

### Preparation of MOF-derived ZnO

A total of 0.5578 g of  $\text{Zn}(\text{NO}_3)_2 \cdot 6\text{H}_2\text{O}$  was placed in beaker A containing 15 mL of methanol, while 0.6157 g of  $\text{C}_4\text{H}_6\text{N}_2$  was placed in beaker B, also containing 15 mL of methanol. Both solutions were stirred magnetically for 30 min to achieve uniform mixing. The solution from beaker A was then quickly poured into beaker B, and the mixture was stirred for ten h at room temperature. Once the reaction finished, a white opaque solution was obtained. The solution was subjected to centrifugation, and the resulting precipitate was rinsed several times with methanol. The sediment was dried in an oven at 60 °C for 24 h to obtain ZIF-8 samples. The ZIF-8 powder was ground, placed into a corundum boat, and heated in a single-temperature zone tube furnace (Thermo Fisher, TF55035C-1). Slowly increase the temperature to 400 °C (2 °C/min) and hold for 2 h in an air atmosphere. After natural cooling, ZIF-8-derived ZnO was obtained.

### Preparation of MOF-derived Co-ZnO

A total of 0.5578 g of  $\text{Zn}(\text{NO}_3)_2 \cdot 6\text{H}_2\text{O}$  and 0.6772 g of  $\text{C}_4\text{H}_6\text{N}_2$  were placed into beakers A and B, each containing 15 mL of methanol. Additionally, 0.0546 g of  $\text{Co}(\text{NO}_3)_2 \cdot 6\text{H}_2\text{O}$  (with a Co to Zn molar ratio of 1:10) was placed in beaker C, which contained 5 mL of methanol. All solutions were magnetically stirred for 30 min to form a uniform mixture. Following the same procedure used for ZIF-8 preparation, Co/Zn-MOF samples were obtained. These samples were then calcined under identical conditions to produce Co-doped porous ZnO materials.

### Preparation of MOF-derived Au@Co-ZnO and Au@ZnO

First, 0.3 g of dry purple Co/Zn-MOF powder was placed in a beaker containing 30 mL of ethanol and stirred with a magnetic stirrer for 30 min to ensure uniform dispersion. Then, 7 mL of chloroauric acid solution (5 mmol/L) was added, and the mixture was stirred for an additional hour to obtain a purplish-blue opaque solution. This solution was centrifuged and washed repeatedly with ethanol. The resulting product was dried in an oven at 60 °C for 24 h, yielding Au@Co/Zn-MOF samples. These samples were then

calcined under the same conditions to produce Au@Co-ZnO (5.41 Wt.% Au). For comparison, ZIF-8 was substituted for Co/Zn-MOF, and the same preparation process was followed to obtain Au@ZIF-8 and gold nanoparticle-modified porous ZnO (Au@ZnO).

### Characterization

The thermogravimetric (TG) analysis curve was obtained by the synchronous thermal analyzer (NETZSCH, Germany, STA449F3) to analyze the thermal stability of the samples. The X-ray diffraction (XRD, D8 Advance instrument, Bruker, Germany) with Cu K $\alpha$  radiation ( $\lambda = 1.5418 \text{ \AA}$ ) was used to analyze the crystal structures of samples. Scanning electron microscopy (SEM, ZEISS, Sigma300), equipped with energy dispersive X-ray spectroscopy [energy dispersive spectroscopy (EDS), smart EDX], was used to characterize the surface morphologies and elemental composition distribution of the samples. The microstructure and crystallographic analysis of samples were characterized by Scanning electron microscopy (TEM) and high-resolution TEM (HRTEM) maps measured by TEM (JEOL, JEM-2100). X-ray photoelectron spectroscopy (XPS, Thermo Fisher, ESCALAB XI+) was used to measure the elemental composition and valence state of the sample surface. The specific surface area and pore size distribution of the samples were measured using the Brunauer-Emmett-Teller (BET) method (Micromeritics, ASAP2020HD88). The band structure of the samples was analyzed by ultraviolet-visible (UV-VIS) absorption spectrum measured by a UV spectrophotometer (SHIMADZU, Japan, UV-3600i Plus).

### Preparation and performance test of gas sensor

The sensitive material powder (Au@Co-ZnO and its comparative samples) was mixed with anhydrous ethanol to prepare a slurry, which was then uniformly coated onto the surface of Au interdigital electrodes. After drying at room temperature, the Au interdigital electrodes covered with the sensitive material were annealed in air at 300 °C for 4 h (heating rate of 5 °C/min), resulting in the fabrication of gas sensors. To improve the repeatability and accuracy of the gas sensing tests, at least three sensor samples were prepared for each sensitive material. A heating layer was integrated on the backside of the Au interdigital electrodes, allowing the operating temperature of the sensors to be controlled by connecting to a heating power supply.

The gas sensing tests were conducted using a custom-built testing system. The gas sensor was soldered onto a four-pin base and connected to a digital source meter (Keithley 2400, Tektronix, USA) and a direct current (DC) heating power supply (KA3003P, Shenzhen Keriyuan Technology Co., Ltd.) for testing. The digital source meter was used to monitor changes in sensor resistance and current, while the DC heating power supply controlled the operating temperature of the sensor. The gas sensing tests were performed by alternately exposing the sensor to cycles of air–target gas–air. A stable voltage was applied to the gas sensor, and sensitivity, response time, and recovery time were calculated by analyzing resistance changes. The resistance measured in air is denoted as air resistance ( $R_a$ ), while the resistance measured in the target gas is referred to as gas resistance ( $R_g$ ). The response value (sensitivity) of the gas sensor is defined as  $R_a/R_g$ . The response time is defined as the time required for the sensor's response value to reach 90% of the stable value after exposure to the target gas, and the recovery time is defined as the time required for the response value to return to 10% of the stable value after the target gas is removed<sup>[22]</sup>.

## RESULTS AND DISCUSSION

As illustrated in [Figure 1A](#), Co/Zn-MOF powder was synthesized via a simple precipitation method at room temperature. Subsequently, Au@Co/Zn-MOF was prepared through ion exchange with chloroauric acid, and Au@Co-ZnO was obtained by high-temperature calcination in air. The oxygen adsorption model shown in [Figure 1B](#) explains the detection mechanism of Au@Co-ZnO for ethanol. When in contact with air, oxygen molecules attach to the surface of the Au@Co-ZnO dodecahedron material and diffuse into its

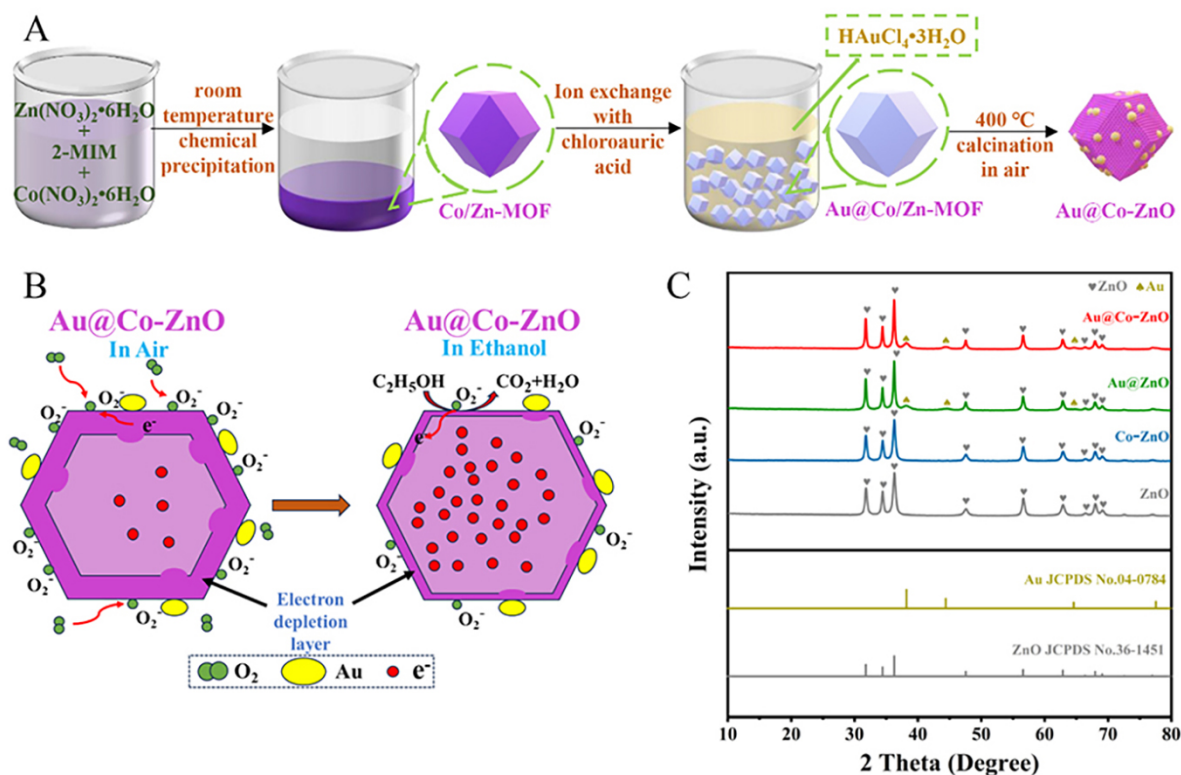


**Figure 1.** We present the preparation process, gas sensing mechanism, and XRD patterns of Au@Co-ZnO nanostructure in Figure 1A-C. A: preparation process of Au@Co-ZnO nanostructure; B: schematic diagram of gas sensing mechanism; C: XRD patterns of Au@Co-ZnO and its comparison samples. XRD: X-ray diffraction.

porous structure. At an optimal working temperature (such as 140 °C), due to the high electronegativity of oxygen, electrons from the conduction band are captured by oxygen molecules, which convert to O<sub>2</sub><sup>-</sup>, leading to an increase in the material's resistance. When in contact with ethanol, the ethanol molecules react with the chemisorbed O<sub>2</sub><sup>-</sup> ions, releasing electrons back into the material and thus decreasing the resistance of Au@Co-ZnO. The gas-sensing performance of the material can be analyzed by calculating the resistance change of the Au@Co-ZnO gas sensor in air and ethanol atmospheres.

The transformation from ZnO to Au@Co-ZnO was confirmed using XRD patterns [Figure 1C]. The XRD patterns of Au@Co-ZnO and its comparison samples are basically consistent with the standard card, and there are no characteristic peaks or impurity peaks of the respective MOF precursors [Supplementary Figure 1A] before calcination, indicating that all MOF precursors have been completely converted to Au@Co-ZnO and its comparative samples after calcination. The XRD pattern of Au@Co-ZnO displays prominent diffraction peaks corresponding to ZnO and Au without any impurity peaks from other oxides. The peaks at  $2\theta = 31.79^\circ, 34.43^\circ, 36.28^\circ, 47.57^\circ, 56.66^\circ, 62.89^\circ, 66.45^\circ, 67.99^\circ,$  and  $69.12^\circ$  correspond to the (100), (002), (101), (102), (110), (103), (200), (112), and (201) crystal planes of ZnO (JCPDS No.36-1451), confirming its hexagonal wurtzite structure<sup>[23]</sup>. Additionally, diffraction peaks at  $2\theta = 38.09^\circ, 44.38^\circ,$  and  $64.76^\circ$  are attributed to the (111), (200), and (220) crystal planes of cubic Au (JCPDS No.04-0784), confirming the reduction of Au<sup>3+</sup> to Au<sup>0</sup>. This demonstrates the successful loading of Au nanoparticles on the ZnO material<sup>[24]</sup>. The three primary diffraction peaks of ZnO in both Co-ZnO and Au@Co-ZnO samples show no shift when compared to ZnO and Au@ZnO. This lack of shift is likely because only a small amount of Co<sup>2+</sup> ions were incorporated into the reaction during the synthesis of the Co/Zn-MOF precursor.

Additionally, the minimal difference between the ionic radii of  $\text{Co}^{2+}$  (0.72 Å) and  $\text{Zn}^{2+}$  (0.74 Å) makes it difficult for the lattice parameters of ZnO to change.

The morphology of Au@Co-ZnO and related samples was characterized using SEM. As shown in [Figure 2A-I](#), the average particle size of ZIF-8 is approximately 300 nm, with a smooth surface and a well-defined rhombohedral structure. After high-temperature calcination, [Figure 2A-II](#) demonstrates that the pyrolysis of the organic framework in ZnO samples results in structural collapse, reducing the average particle size to about 250 nm. The material's edges consist of numerous primary nanoparticles, and its surface becomes notably rough with pronounced depressions. The Co-ZnO material used as a comparison sample retains a similar dodecahedral framework [[Figure 2A-III](#)].

**Figure 2.** SEM images, EDS face scan energy spectra, TEM and HRTEM images of Au@Co-ZnO nanostructure and its contrast samples. A-I: SEM image of ZIF-8; A-II: SEM image ZnO; A-III: SEM image Co-ZnO; A-IV: SEM image Au@ZIF-8; A-V: SEM image Au@ZnO; A-VI: EDS face scan energy spectra of Au@ZnO; B-I: SEM image Au@Co/Zn-MOF; B-II: SEM image Au@Co-ZnO; B-(III-VII): EDS face scan energy spectra of Au@Co-ZnO; C-I: TEM images of Au@Co-ZnO; C-VV: HRTEM images of Au@Co-ZnO. SEM: scanning electron microscopy; EDS: energy dispersive spectroscopy; MOF: metal-organic framework; TEM: transmission electron microscopy; HRTEM: high-resolution transmission electron microscopy.

The morphology of the Au@ZIF-8 sample obtained after ion exchange has not changed significantly, and it still has a polyhedral structure [[Figure 2A-IV](#)]. After high-temperature calcination, the surface of Au@ZnO becomes rough, but no serious depression occurs and the collapse degree is relieved to a certain extent [[Figure 2A-V](#)]. Similarly, the morphology and structure of the Au@Co/Zn-MOF sample [[Figure 2B-I](#)] are consistent with those of ZIF-8. As shown in [Figure 2B-II](#), Au@Co-ZnO samples exhibit a polyhedral structure with numerous pores, and structural collapse resulting from the removal of organic linkers has been significantly alleviated, which is consistent with the TG analysis results [[Supplementary Figure 1B-D](#)]. When the temperature reaches 400 °C, the weight loss of Au@Co/Zn-MOF precursor is only 2.8% [[Supplementary Figure 1D](#)], a notable decrease compared to 7.7% of the ZIF-8 sample [[Supplementary Figure 1B](#)] and 5.1% for Co/Zn-MOF [[Supplementary Figure 1C](#)], indicating enhanced thermal stability of the material. This improvement may be attributed to the ion exchange between  $\text{Au}^{3+}$  and  $\text{Zn}^{2+}$ , along with the dispersion of  $\text{Au}^{3+}$  ions within the interstitial spaces of the MOF during agitation, which enhances the structural stability of the precursor<sup>[25]</sup>. At the same time, there are a large number of random nanoparticle aggregates around the polyhedron, which may be formed by the collapse and condensation of the precursor with a small growth structure during heat treatment or the formation of gold nanoparticles of uneven size. The EDS test results of Au@ZnO and Au@Co-ZnO shown in [Figure 2A-VI](#) and [Figure 2B-\(III-VII\)](#), Zn, Co, O are evenly distributed in the display area, but Au is not evenly distributed and there is an obvious agglomerating phenomenon.

The morphology and structure of Au@Co-ZnO were further analyzed using TEM. As shown in [Figure 2C-I](#), numerous nanoparticles of uneven sizes are dispersed and attached to the main material in the Au@Co-ZnO. The HRTEM images [[Figure 2C-II](#)] reveal two types of lattice fringes with different spacings within the sample. The lattice fringes with a spacing of 0.238 nm correspond to the (111) crystal face of cubic-phase Au, while the lattice fringes with a spacing of 0.26 nm are associated with the (002) crystal face of the hexagonal wurtzite structure of ZnO. These results further confirm that gold nanoparticles have been successfully loaded onto the Co-doped ZnO polyhedron via cation exchange and subsequent high-temperature calcination.

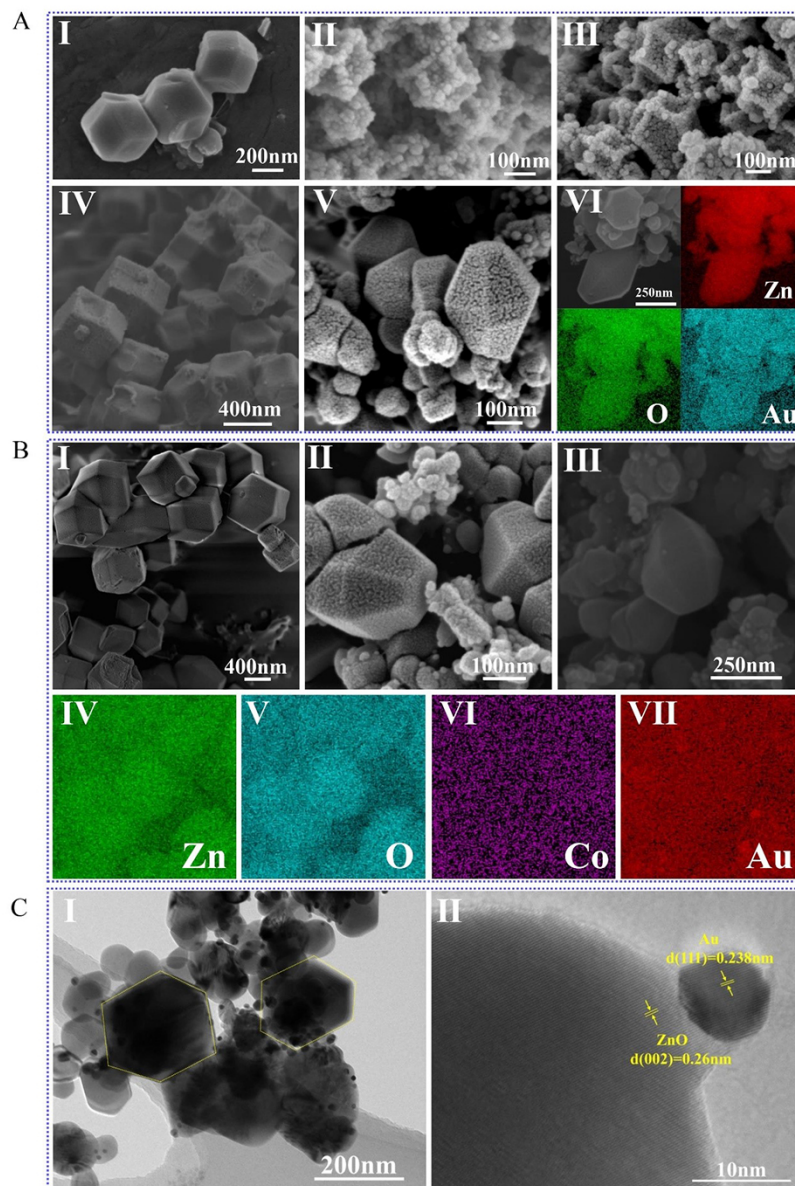


**Figure 2.** SEM images, EDS face scan energy spectra, TEM and HRTEM images of Au@Co-ZnO nanostructure and its contrast samples. A-I: SEM image of ZIF-8; A-II: SEM image ZnO; A-III: SEM image Co-ZnO; A-IV: SEM image Au@ZIF-8; A-V: SEM image Au@ZnO; A-VI: EDS face scan energy spectra of Au@ZnO; B-I: SEM image Au@Co/Zn-MOF; B-II: SEM image Au@Co-ZnO; B-(III-VII): EDS face scan energy spectra of Au@Co-ZnO; C-I: TEM images of Au@Co-ZnO; C-VV: HRTEM images of Au@Co-ZnO. SEM: scanning electron microscopy; EDS: energy dispersive spectroscopy; MOF: metal-organic framework; TEM: transmission electron microscopy; HRTEM: high-resolution transmission electron microscopy.

The Au@Co-ZnO samples were analyzed using XPS to determine the surface elemental composition and chemical states. [Figure 3A](#) presents the full spectrum of the Au@Co-ZnO sample. Consistent with EDS results, the elements Zn, O, Co, and Au are identified on the sample's surface. In the high-resolution energy spectra of Zn [[Figure 3B](#)], the characteristic peaks with binding energies of 1021.5 eV and 1044.4 eV correspond to the Zn 2p<sub>3/2</sub> and Zn 2p<sub>1/2</sub> levels of ZnO, respectively. The energy difference between these two peaks is approximately 23 eV, confirming the presence of Zn<sup>2+</sup> in the Au@Co-ZnO samples<sup>[26]</sup>. In addition, XPS analysis of pure ZnO and Co-ZnO is also performed, and similar results are obtained [[Supplementary](#)

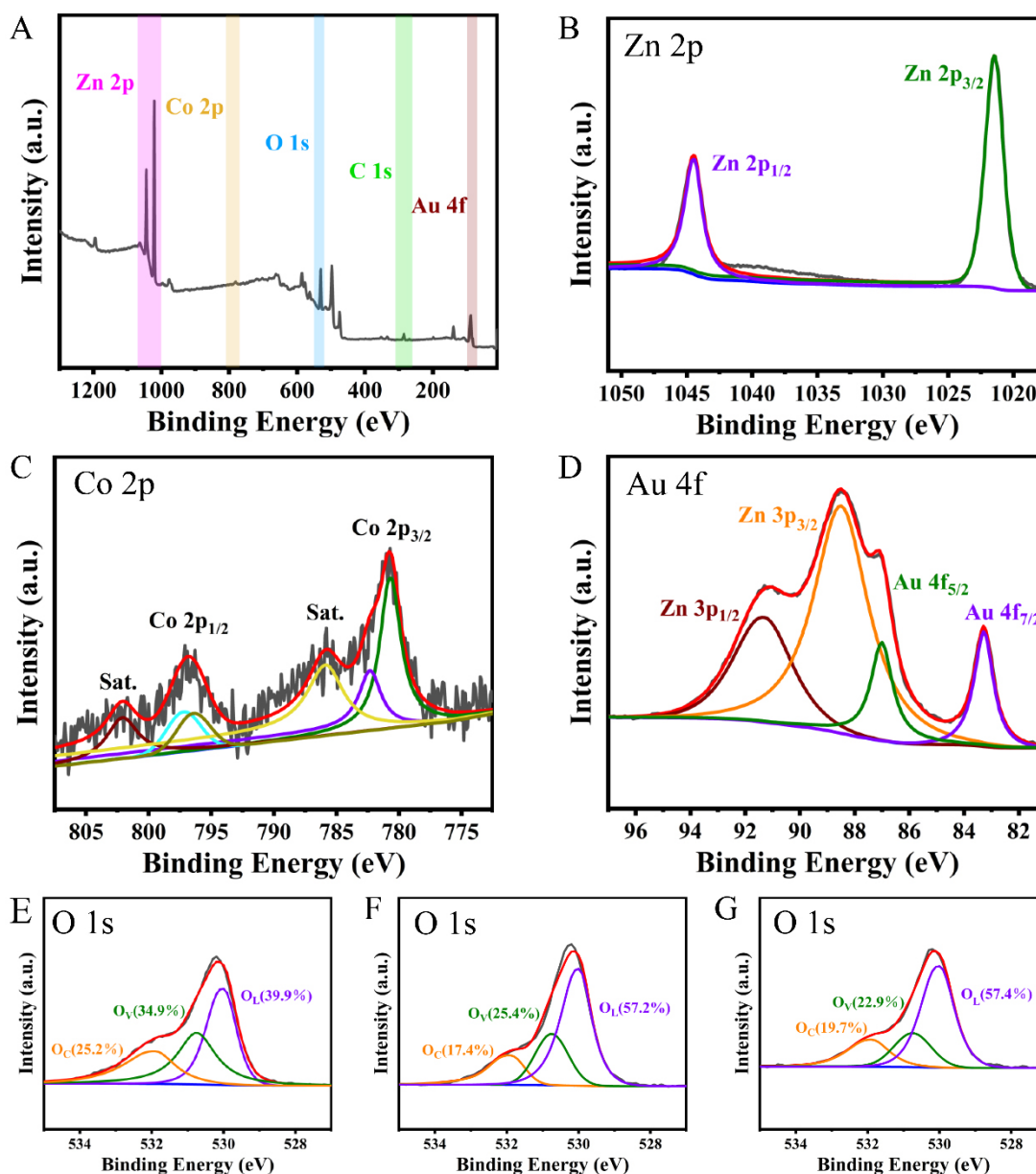


**Figure 3.** XPS spectra of Au@Co-ZnO nanostructure and high-resolution spectra of O 1s of different samples. A: full spectrum of Au@Co-ZnO; B: high-resolution spectra of Zn 2p of Au@Co-ZnO; C: high-resolution spectra of Co 2p of Au@Co-ZnO; D: high-resolution spectra of Au 4f of Au@Co-ZnO; E: high-resolution spectra of O 1s of Au@Co-ZnO; F: high-resolution spectra of O 1s of Co-ZnO; G: high-resolution spectra of O 1s of ZnO. XPS: X-ray photoelectron spectroscopy.

Figure 2 and Supplementary Figure 3].

The Co 2p spectrum of the Au@Co-ZnO sample [Figure 3C] reveals one main peak, one shoulder, and two satellite peaks. The main peak and shoulder, observed at binding energies of 780.8 eV and 796.8 eV, are attributed to Co 2p<sub>3/2</sub> and Co 2p<sub>1/2</sub>, respectively. The energy difference between these peaks is approximately 16 eV, which aligns with literature reports, effectively confirming the presence of Co<sup>2+</sup> in the material and its incorporation into the lattice structure<sup>[27,28]</sup>. As illustrated in Figure 3D, the characteristic binding energies for Au 4f<sub>7/2</sub> and Au 4f<sub>5/2</sub> are 83.3 eV and 87.0 eV, respectively, with a peak difference of 3.7 eV. This is

consistent with the standard value for spin-orbit doublet separation, further confirming the existence of Au<sup>0</sup> in the Au@Co-ZnO sample<sup>[29-31]</sup>. In addition, compared to the binding energies of the standard Au 4f peaks (84.0 eV and 87.7 eV), the characteristic peaks of the Au@Co-ZnO sample shift to lower energy levels, which is contrary to the change observed in the Zn 2p peaks. This shift results from electron interactions caused by the transfer of electrons from ZnO to Au<sup>[32]</sup>. The two interference peaks at 88.5 eV and 91.4 eV correspond to Zn 3p<sub>3/2</sub> and Zn 3p<sub>1/2</sub> in ZnO, respectively. In the O 1s high-resolution energy spectrum shown in [Figure 3E](#), the three characteristic peaks with binding energy at 530.0 eV, 530.8 eV and 531.9 eV are attributed to lattice oxygen (O<sub>L</sub>), oxygen vacancies (O<sub>V</sub>) and adsorbed oxygen (O<sub>C</sub>), respectively. The increased proportion of O<sub>V</sub> in the material significantly enhances its gas-sensitive properties. The proportion of O<sub>V</sub> in the Au@Co-ZnO sample is 34.9%, significantly higher than 25.4% in Co-ZnO [[Figure 3F](#)] materials and 22.9% in pure ZnO materials [[Figure 3G](#)]. Therefore, the Au@Co-ZnO sample may have better detection capability for ethanol.

The specific surface area and abundant void channels are critical factors influencing the gas-sensitive properties of materials. The specific surface area and pore size distribution of Au@Co-ZnO and its comparative samples were determined using nitrogen adsorption and desorption isotherms, as illustrated in [Figure 4A-D](#). All samples exhibit typical type IV nitrogen adsorption/desorption isotherms, indicating mesoporous structures with pore sizes predominantly ranging from 5 nm to 40 nm. The specific surface areas of pure ZnO, Co-ZnO, Au@ZnO, and Au@Co-ZnO samples are 15.55 m<sup>2</sup>/g, 29.00 m<sup>2</sup>/g, 24.03 m<sup>2</sup>/g, and 39.35 m<sup>2</sup>/g, respectively. This data indicates that Co doping and the loading of gold nanoparticles significantly enhance the specific surface area of the materials. According to the illustrations in [Figure 4A-D](#), the average desorption pore sizes of pure ZnO, Co-ZnO, Au@ZnO, and Au@Co-ZnO samples are 28.69 nm, 20.67 nm, 13.84 nm, and 11.41 nm, respectively. Notably, the average pore diameter of the gold-loaded materials significantly decreased compared to pure ZnO. This reduction in average pore size can be attributed to two factors: first, the enhanced thermal stability of the precursor, which leads to a relatively weak structural collapse of the Au@Co-ZnO material during the removal of organic linkers, resulting in smaller pores formed from the pyrolysis of the organic skeleton. Secondly, the irregular size of gold nanoparticles, randomly distributed on the surface of the polyhedron, partially blocks the material's pore channels.

The operating temperature of gas-sensitive materials significantly influences the sensing performance of gas sensors<sup>[33]</sup>. Therefore, the optimal operating temperature of the Au@Co-ZnO sample was first investigated. As illustrated in [Figure 5A](#), the response value of all samples to 100 ppm ethanol initially increases and then decreases with rising temperature. This pattern arises because the adsorption and desorption rates of gas molecules, as well as the reactivity of ethanol molecules, are temperature-dependent<sup>[34]</sup>. At the optimal working temperature, the adsorption and desorption rates of ethanol molecules on the surface of the gas-sensitive material reach equilibrium, and the redox reaction rate between chemisorbed oxygen ions and ethanol molecules is maximized, leading to the highest sensitivity for the sample. As shown in [Figure 5A](#), the response value of the Au@Co-ZnO sample to 100 ppm ethanol at 140 °C is 205.3, which represents a significant enhancement compared to that of the pure ZnO sample (7.1) by a factor of 28.9, the Co-ZnO sample (114.6) by a factor of 1.8, and the Au@ZnO sample (91.1) by a factor of 2.3, respectively. This demonstrates its outstanding responsiveness to ethanol gas. Furthermore, the optimal working temperature of the Au@Co-ZnO sample (140 °C) is 40 °C lower than that of the pure ZnO sample (180 °C). This reduction in operating temperature can be attributed to the decreased activation energy of the redox reaction due to noble metal modification and Co doping into the ZnO lattice. A lower operating temperature is advantageous in reducing overall power consumption in practical applications. As shown in [Figure 5B-D](#), at their respective optimal operating temperatures, the responses to 100 ppm ethanol are 19.1

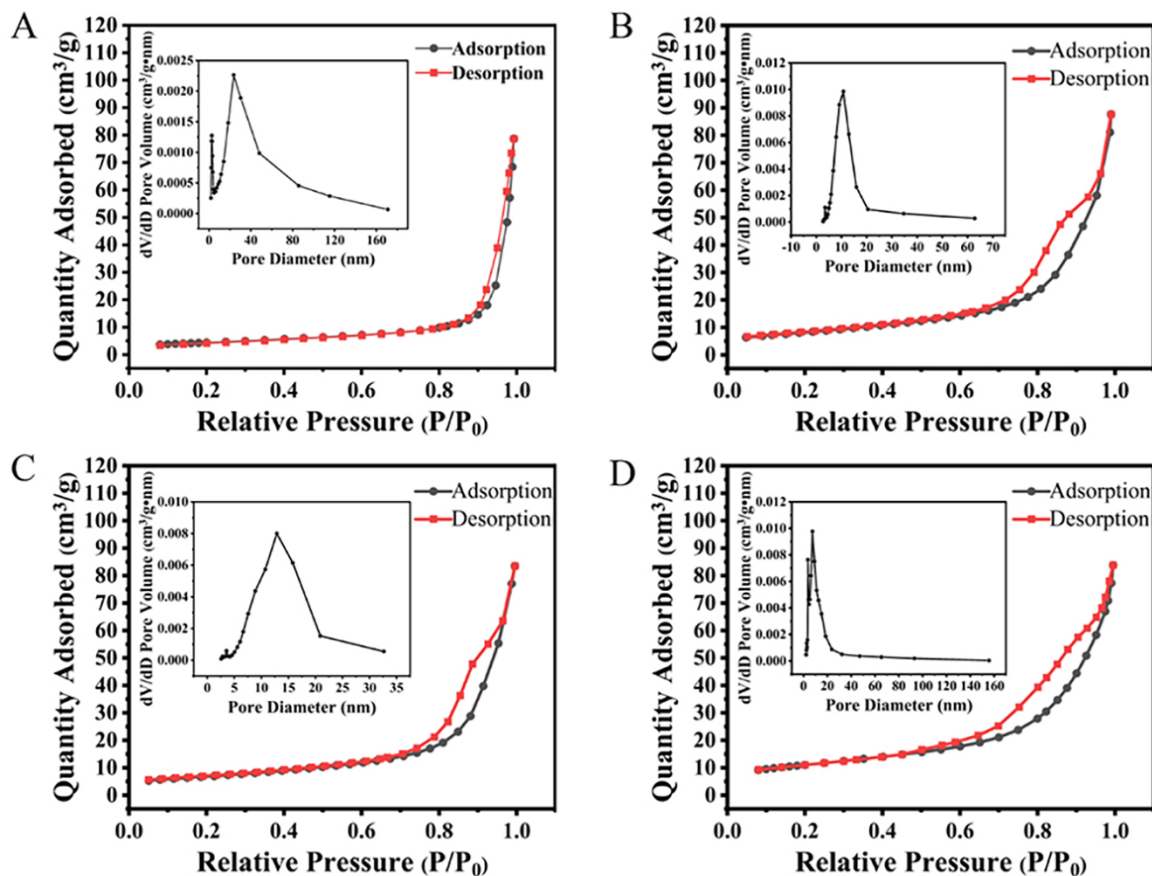


**Figure 4.** The nitrogen adsorption and desorption isothermal curves of Au@Co-ZnO nanostructure and its contrast samples. A: pure ZnO; B: Co-ZnO; C: Au@ZnO; D: Au@Co-ZnO. The insets are the pore size distribution curves of the corresponding samples.

for pure ZnO, 113.4 for Co-ZnO, and 205.3 for Au@Co-ZnO, indicating significant improvement. The Au@Co-ZnO sample has a response time of 28 s and a recovery time of 10 s. Its longer response time compared to the pure ZnO sample may be due to the lower working temperature, which slows down the adsorption rate of ethanol gas.

The dynamic response-recovery test was conducted for varying concentrations of ethanol gas at the respective optimal operating temperatures of the samples. As shown in Figure 5E, the response value of all samples steadily increased with increasing ethanol concentration. Throughout the test, the response value of the Au@Co-ZnO samples was consistently higher than that of the comparison samples. The inset of Figure 5E shows the continuous response-recovery curve of Au@Co-ZnO and its comparison samples under low ethanol gas concentrations (0.2 ppm to 10 ppm), which follows the same trend as at higher ethanol concentrations. Based on the response value at various ethanol concentrations in Figure 5E, the response value-concentration curve, as shown in Figure 5F, was obtained. The response values of the Au@Co-ZnO sample to ethanol gas concentrations of 0.2, 0.5, 1, 5, 10, 20, 40, 60, 80, 100, and 200 ppm were 1.1, 1.3, 2.2, 6.4, 10.9, 31.5, 62.7, 100.8, 159.6, 202.2, and 424.9, respectively. While the performance of Au@Co-ZnO is similar to that of the other two samples for detecting low concentrations of ethanol gas, it outperforms them at higher concentrations. According to  $\log(S) = \log(C) + b^{[35]}$ , where  $S$  is the sensor's response value and  $C$  is the ethanol concentration, the correlation between the response value and the concentration of ethanol can be determined, with  $a$  and  $b$  being constants. After linear fitting of the

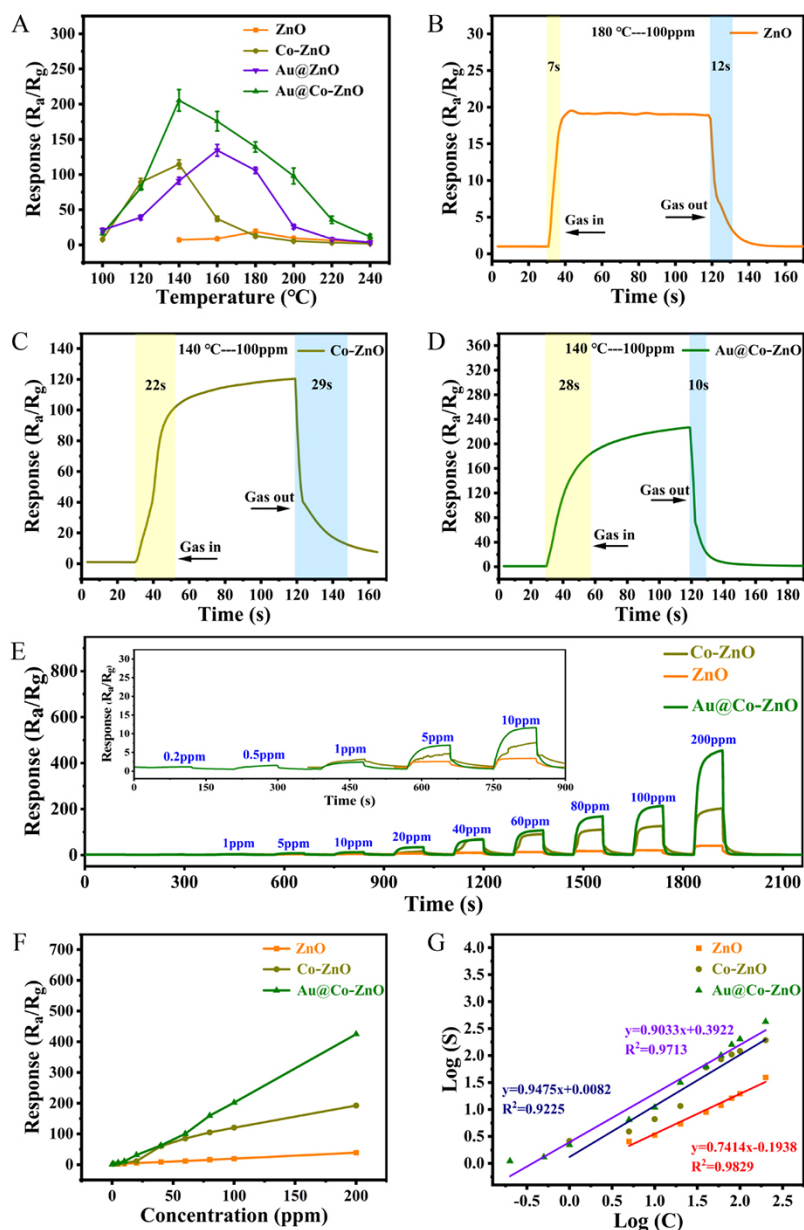


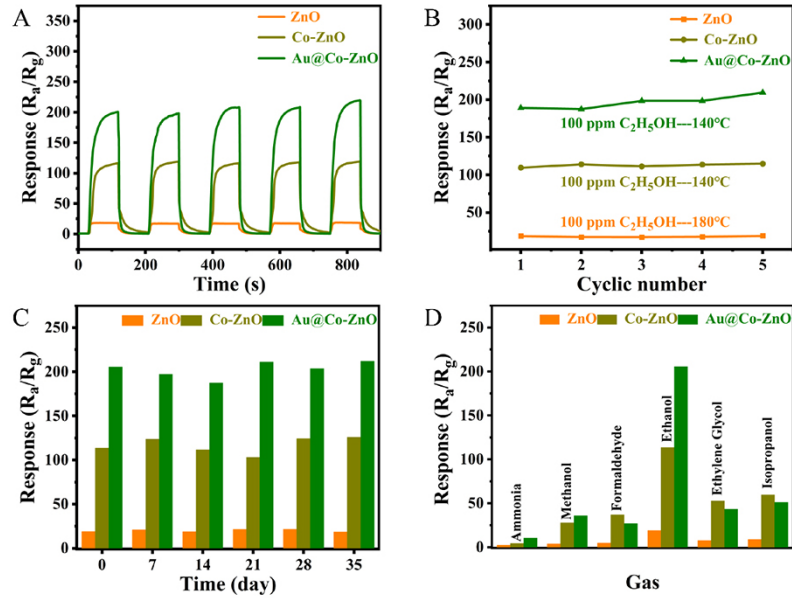
**Figure 5.** Gas sensitivity test results of Au@Co-ZnO nanostructure and its contrast samples in ethanol gas. A: temperature dependence curves of Au@Co-ZnO and its comparison samples on 100 ppm ethanol; B: response-recovery curves of pure ZnO to 100 ppm ethanol at 180 °C; C: response-recovery curves of pure Co-ZnO to 100 ppm ethanol at 140 °C; D: response-recovery curves of pure Au@Co-ZnO to 100 ppm ethanol at 140 °C; E: the continuous response-recovery curves of Au@Co-ZnO and its comparison samples to different concentrations of ethanol gas, illustrated is a local amplification of the continuous response-recovery curves of ethanol concentration from 0.2ppm to 10ppm; F: response value-concentration curves of Au@Co-ZnO and its comparison samples; G: response value-concentration linear fitting curves of Au@Co-ZnO and its comparison samples.

dispersion point [Figure 5G], the fitting line representing Au@Co-ZnO material is  $y = 0.9033x + 0.3922$ , where the correlation coefficient  $R^2 = 0.9713$ . This demonstrates a strong linear correlation between the sensor's sensitivity and the concentration of ethanol.

Compared to pure ZnO, the Co-doped porous ZnO material modified with gold nanoparticles demonstrates significantly improved ethanol sensing performance for several reasons. Firstly, Au@Co-ZnO exhibits a larger specific surface area, offering more active sites for the adsorption and reaction of gas molecules. Additionally, XPS results reveal that Au@Co-ZnO contains a higher concentration of  $O_v$ , resulting in more chemisorbed oxygen ( $O^{\cdot-}$ ) on the material's surface when exposed to air. This contributes to a greater change in resistance before and after ethanol exposure. Secondly, the introduction of  $Co^{2+}$  ions into the ZnO crystal lattice creates electron donor defects ( $CoZn\cdot$ ). Due to cobalt's ability to form higher valence states, more electrons are released compared to  $Zn^{3+}$ , increasing the concentration of free electrons on the material's surface and facilitating the adsorption of oxygen. In addition, the UV-VIS absorption spectrum tests [Supplementary Figure 4A and B] indicate that the band gap of Co-doped porous ZnO (3.17 eV) is smaller than that of pure ZnO (3.23 eV), promoting electron transitions and raising the electron concentration in the conduction band at the same temperature. This allows Co-ZnO gas-sensitive materials to exhibit excellent ethanol detection at lower operating temperatures. Finally, the chemical sensitization and electron sensitization effects of gold nanoparticles further improve the performance of gas-sensitive materials<sup>[21]</sup>. Due to chemical sensitization effect, gold nanoparticles facilitate the dissociation of oxygen molecules into more reactive adsorbed oxygen species, which increases chemisorbed oxygen on the surface of Au@Co-ZnO and enhances its reactivity with ethanol. Moreover, due to the different work functions of ZnO and Au, an electron sensitization effect occurs. As shown in Supplementary Figure 5A and B, a Schottky barrier forms at the interface between Co-ZnO and Au when they come into contact, causing electrons to transfer from the Co-ZnO conduction band to the gold nanoparticles. This process widens the electron depletion layer of the Au@Co-ZnO material, resulting in a more pronounced change in resistance before and after ethanol exposure, further improving its sensing capabilities.

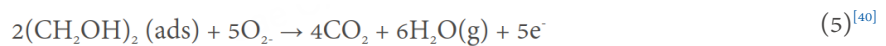
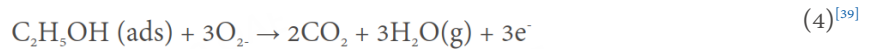
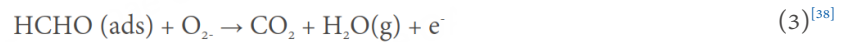
To evaluate the stability of Au@Co-ZnO material and its comparison samples for ethanol detection, dynamic cyclic stability tests were conducted over five consecutive cycles at their respective optimal operating temperatures, each with a duration of 180 seconds [Figure 6A]. The results indicated slight fluctuations across all samples. The response values for each ethanol gas injection cycle, as shown in the response value-cycle number curve [Figure 6B], reveal that the Au@Co-ZnO sample exhibited values of 189.0, 187.4, 198.4, 198.4, and 209.4, respectively. This indicates that there is still potential for improvement in its short-term repeatability for ethanol detection. In addition to short-term stability, long-term stability is a crucial factor for evaluating the gas-sensing performance of materials, as it influences the service life of the sensor. During a 35-day test period, the response values of Au@Co-ZnO material to 100 ppm ethanol were 205.3, 197.2, 187.2, 211.5, 203.7, and 212.4 [Figure 6C]. Compared to the initial response value of 205.3 obtained in the earlier temperature-dependent test, the fluctuation in response value over this period was less than 9%. For comparison, the fluctuation ranges for pure ZnO and Co-ZnO materials were less than 15% and 11%, respectively, indicating that Au@Co-ZnO offers relatively superior long-term stability for ethanol gas detection.

Figure 6D reflects the response of all samples to different reducing gases at their respective optimum operating temperatures. The results show that all three samples exhibit the highest response to ethanol gas under the same external light and humidity conditions. The response value of the Au@Co-ZnO sample to ethanol is 205.3, which is 19.3 times that of ammonia (10.6), 5.7 times that of methanol (35.8), 7.6 times that of formaldehyde (26.9), 4.7 times that of ethylene glycol (43.4) and 4.0 times that of isopropyl alcohol (50.9), respectively. In addition, the ethanol selectivity of Au@Co-ZnO is better than that of pure ZnO and Co-ZnO samples.



**Figure 6.** Stability and gas selectivity results of Au@Co-ZnO nanostructure and its comparison samples. A: cyclic stability test for 100 ppm ethanol; B: response-cycle number curve; C: long-term stability test; D: response to different gases.

Au@Co-ZnO shows strong selectivity for ethanol, which is related to the redox reaction between ethanol molecules and chemisorbed oxygen ions, the dynamic diameter and the lowest unoccupied molecular orbital (LUMO) energy of ethanol, the gas adsorption capacity and the bond dissociation energy of the gas-sensitive material.



As indicated by formulas 1-6, when the device is exposed to gases such as ammonia, methanol, and formaldehyde, ethanol molecules release more electrons during the chemical reaction, resulting in a greater change in the resistance of the gas-sensitive material. Additionally, the kinetic diameter of ethanol

molecules, approximately 4.3 Å, allows for efficient adsorption and diffusion through the abundant pore channels of porous materials<sup>[42]</sup>. Furthermore, compared with LUMO energies of methanol, formaldehyde and other gases, the LUMO energy of ethanol is only 0.12575 eV, much lower than that of other interfering gases. The higher the LUMO energy value of a gas, the lower the sensitivity of the device to that gas<sup>[35,43,44]</sup>.

The Co-doped porous ZnO materials modified with gold nanoparticles, as prepared in this study, exhibit excellent ethanol sensing properties. When compared with the previously reported data on ZnO-based gas sensors, summarized in Table 1, the Au@Co-ZnO samples demonstrate a relatively lower optimal operating temperature, along with a higher sensitivity and faster response time to ethanol gas.

## CONCLUSIONS

In conclusion, we initially prepared Co/Zn-MOF materials via chemical precipitation at room temperature. Subsequently, we successfully synthesized a MOF-derived porous Au@Co-ZnO nanostructure that maintains the structural characteristics of ZIF-8, featuring a high specific surface area and abundant pores, through ion exchange and calcination of the Co/Zn-MOF material. The response value of the Au@Co-ZnO material to 100 ppm ethanol at the optimal operating temperature (140 °C) reaches 205.3, with response and recovery times of 28 s and 10 s, respectively. This material demonstrates excellent performance in detecting high concentrations of ethanol gas. Additionally, the gas-sensitive material exhibits long-term stability and good selectivity for ethanol. Compared to the summarized reported data on ZnO-based gas sensors, the MOF-derived porous Au@Co-ZnO nanostructure samples have a relatively lower optimal operating temperature, while also providing a higher sensitivity and faster response time to ethanol gas. In summary, the MOF-derived porous Au@Co-ZnO nanostructures we prepared exhibit promising potential in ethanol gas sensing applications. This also demonstrates the effectiveness of the synergistic effects of heterometallic element doping and noble metal loading in improving the performance of metal oxide semiconductor-based gas sensors. However, challenges remain in practical applications, such as the high cost of Au and the relatively elevated operating temperature (140 °C). Future efforts could focus on replacing Au with more cost-effective noble metals (e.g., Ag) to reduce costs, employing co-doping with multiple heterometallic elements, or developing composite materials with room-temperature sensitive materials (e.g., MXene) to further lower the operating temperature.

**Table 1. Comparison of ethanol sensing performance of different ZnO-based gas sensors**

Material	T (°C)	C (ppm)	Response	Tres/trec (s)	Ref.
Derived Co <sub>3</sub> O <sub>4</sub> /ZnO nanostructures	300	10	34.9	57/235	[45]
CuO-ZnO/g-C <sub>3</sub> N <sub>4</sub>	260	500	16	87/169	[46]
ZnO-Co <sub>3</sub> O <sub>4</sub>	200	1000	106	7/236	[47]
CuO/ZnO	300	100	28	2/72	[48]
Au/ZnO	250	100	37.74	19/9	[25]
ZnO@In <sub>2</sub> O <sub>3</sub>	200	100	269.1	18/35	[42]
Ag@ZnO	75	100	41.1	10/50	[49]
Au@Co-ZnO	140	100	205.3	28/10	This work

## DECLARATIONS

### Authors' contributions

Conceived and designed the study: Fu, Y.; Tian, K.

Prepared the samples and collected the data: Tian, K. W.; Fu, Y. K.; Xiong, G. J.

Performed data analysis and wrote the main draft of the paper: Tian, K.; Fu, Y.; Kuang, S.

Literature search and organization: Zhao, Z.; Zhou, T.

provided technical, and material support: Xiong, L.

Advising the scientific discussion on this research and manuscript revision: Kuang, S.; Haq, I.; Xiong, L.; Weng,; Peng, X.

All authors participated in the writing of the manuscript.

### Availability of data and materials

The data supporting the findings of this study are available within this Article and its Supplementary Information. According to reasonable requirements, all the data examined in this research can be obtained from the correspondents.

### Financial support and sponsorship

This work was partially supported by the “Key Project of Science and Technology Research Program of Hubei Provincial Department of Education” [F2023008], the “Graduate Innovative Fund of Wuhan Institute of Technology” [NO: CX2023093], and the “Youth Project of Natural Science Foundation of Hubei Province” [Grant No. 2023AFB224].

### Conflicts of interest

Liwei Xiong is an Assistant Guest Editor of the Special Issue on “Structural Regulation and Application of Two-Dimensional Metal Oxides” but was not involved in any steps of editorial processing, notably including reviewer selection, manuscript handling, or decision-making. The other authors declare that there are no conflicts of interest.

### Ethical approval and consent to participate

Not applicable.

### Consent for publication

Not applicable.

### Copyright

© The Author(s) 2025.

## REFERENCES

1. Shi, Y.; Li, X.; Sun, X.; Shao, X.; Wang, H. Strategies for improving the sensing performance of In<sub>2</sub>O<sub>3</sub>-based gas sensors for ethanol detection. *J. Alloys. Compd.* **2023**, *963*, 171190. DOI
2. Comini, E. Metal oxide nano-crystals for gas sensing. *Anal. Chim. Acta.* **2006**, *568*, 28-40. DOI PubMed
3. Bakker, E.; Telling-Diaz, M. Electrochemical sensors. *Anal. Chem.* **2002**, *74*, 2781-800. DOI PubMed
4. Kim, H.; Uddin, S. Z.; Lien, D. H.; et al. Actively variable-spectrum optoelectronics with black phosphorus. *Nature* **2021**, *596*, 232-7. DOI
5. Ma, N.; Ide, S.; Suematsu, K.; Watanabe, K.; Shimano, K. Novel solid electrolyte CO<sub>2</sub> gas sensors based on *c*-Axis-oriented Y-doped La<sub>0.66</sub>Si<sub>5.3</sub>B<sub>0.7</sub>O<sub>26.14</sub>. *ACS. Appl. Mater. Interfaces.* **2020**, *12*, 21515-20. DOI PubMed
6. Hyodo, T.; Hiura, T.; Nagae, K.; Ueda, T.; Shimizu, Y. Effects of catalytic combustion behavior and adsorption/desorption properties on ethanol-sensing characteristics of adsorption/combustion-type gas sensors. *J. Asian. Ceram. Soc.* **2021**, *9*, 1015-30. DOI
7. Mirzaei, A.; Ansari, H. R.; Shahbaz, M.; Kim, J.; Kim, H. W.; Kim, S. S. Metal oxide semiconductor nanostructure gas sensors with different morphologies. *Chemosensors* **2022**, *10*, 289. DOI
8. Kgomo, M. B.; Swart, H. C.; Mhlongo, G. H. Engineering of mesoporous cube-like In<sub>2</sub>O<sub>3</sub> products as ethanol detection platform at low operating temperature: effects of different transition metals as dopant ions. *ACS. Omega.* **2024**, *9*, 6325-38. DOI PubMed PMC
9. Xin, J.; Wang, W.; Xie, L.; et al. MOF-derived Al<sup>3+</sup>-doped Co<sub>3</sub>O<sub>4</sub> nanocomposites for highly n-butanol gas sensing performance at low operating temperature. *J. Alloys. Compd.* **2024**, *978*, 173341. DOI
10. Ma, C.; Yang, Q.; Su, H.; Yang, H.; Wang, X.; Zeng, D. Cu-MOF-derived C-doped CuO/Cu<sub>2</sub>O hollow nano-octahedrons for room-temperature NO<sub>2</sub> sensing at the ppb level. *ACS. Appl. Nano. Mater.* **2024**, *7*, 3105-15. DOI
11. He, F.; Zhang, Y.; Chen, H.; et al. Highly sensitive and selective gas sensor based on SnO<sub>2</sub>/Fe<sub>2</sub>O<sub>3</sub>@rGO nanocomposite for detection of formaldehyde. *Mater. Chem. Phys.* **2024**, *312*, 128646. DOI
12. Yang, Q.; Wu, Y.; Liu, Y.; Pan, C.; Wang, Z. L. Features of the piezo-phototronic effect on optoelectronic devices based on wurtzite semiconductor nanowires. *Phys. Chem. Chem. Phys.* **2014**, *16*, 2790-800. DOI
13. Li, L.; Zhang, Y.; Wang, R.; et al. Ferroelectricity-induced performance enhancement of V-doped ZnO/Si photodetector by direct energy band modulation. *Nano. Energy.* **2019**, *65*, 104046. DOI
14. Anjana, R.; Subha, P. P.; Kurias, M. K.; Jayaraj, M. K. Enhanced green upconversion luminescence in ZnO: Er<sup>3+</sup>, Yb<sup>3+</sup> on Mo<sup>6+</sup> co-doping for temperature sensor application. *Methods. Appl. Fluoresc.* **2017**, *6*, 015005. DOI PubMed
15. Cao, L.; Kiely, J.; Piano, M.; Luxton, R. Nanoparticle-based 3D membrane for impedimetric biosensor applications. *Bioelectrochemistry* **2020**, *136*, 107593. DOI PubMed
16. Du, G.; Feng, P.; Cheng, X.; Li, J.; Luo, X. Immobilizing of ZIF-8 derived ZnO with controllable morphologies on zeolite A for efficient photocatalysis. *J. Solid. State. Chem.* **2017**, *255*, 215-8. DOI
17. Ren, X.; Xu, Z.; Liu, D.; Li, Y.; Zhang, Z.; Tang, Z. Conductometric NO<sub>2</sub> gas sensors based on MOF-derived porous ZnO nanoparticles. *Sens. Actuators. B.: Chem.* **2022**, *357*, 131384. DOI
18. Bulemo, P. M. Ga-doped ZnO microbelts based resistive-type sensor for detection of acetylene gas. *ACS. Appl. Electron. Mater.* **2023**, *5*, 2106-14. DOI
19. Dai, H.; Ding, J.; Chen, H.; Fu, H. Improvement of ethanolamine sensing performance based on Au-modified ZnO rod-like nanoflowers. *Mater. Lett.* **2023**, *340*, 134183. DOI
20. Xu, J.; Li, S.; Li, L.; Chen, L.; Zhu, Y. Facile fabrication and superior gas sensing properties of spongelike Co-doped ZnO microspheres for ethanol sensors. *Ceram. Int.* **2018**, *44*, 16773-80. DOI
21. Zhu, L.; Zeng, W. Room-temperature gas sensing of ZnO-based gas sensor: a review. *Sens. Actuators. A.: Phys.* **2017**, *267*, 242-61. DOI
22. Cao, S.; Song, Z.; Bing, Y.; Xu, X.; Zhou, T.; Zhang, T. Metal-organic-framework derived Co-Mo multimetal oxide semiconductors: selective trace-level hydrogen sulfide detection. *ACS. Sens.* **2024**, *9*, 2979-88. DOI
23. Phuoc, P. H.; Viet, N. N.; Thong, L. V.; et al. Comparative study on the gas-sensing performance of ZnO/SnO<sub>2</sub> external and ZnO-SnO<sub>2</sub> internal heterojunctions for ppb H<sub>2</sub>S and NO<sub>2</sub> gases detection. *Sens. Actuators. B.: Chem.* **2021**, *334*, 129606. DOI
24. Yang, H.; Zhang, S.; Li, M.; et al. Hollow Au-ZnO/CN nanocages derived from ZIF-8 for efficient visible-light-driven hydrogen evolution from formaldehyde alkaline solution. *Eur. J. Inorg. Chem.* **2019**, *2019*, 2761-7. DOI
25. Kang, Y.; Zhang, L.; Wang, W.; Yu, F. Ethanol sensing properties and first principles study of Au supported on mesoporous ZnO derived from metal organic framework ZIF-8. *Sensors. (Basel).* **2021**, *21*, 4352. DOI PubMed PMC
26. Wang, Z.; Yang, X.; Sun, C.; et al. Excellent acetone sensing performance of Au NPs functionalized Co<sub>3</sub>O<sub>4</sub>-ZnO nanocomposite. *Sens. Rev.* **2022**, *42*, 638-47. DOI
27. Kamble, V. S.; Navale, Y. H.; Patil, V. B.; Desai, N. K.; Vajekar, S. N.; Salunkhe, S. T. Studies on structural, spectral and morphological properties of co-precipitation derived Co-doped ZnO nanocapsules for NO<sub>2</sub> sensing applications. *J. Mater. Sci.: Mater. Electron.* **2021**, *32*, 26503-19. DOI
28. Peng, H.; Liu, F.; Liu, X.; et al. Effect of transition metals on the structure and performance of the doped carbon catalysts derived from polyaniline and melamine for ORR application. *ACS. Catal.* **2014**, *4*, 3797-805. DOI
29. Duan, D.; Hao, C.; He, G.; et al. Co<sub>3</sub>O<sub>2</sub> Nanosheet/Au Nanoparticle/CeO<sub>2</sub> nanorod composites as catalysts for CO oxidation at room temperature. *ACS. Appl. Nano. Mater.* **2020**, *3*, 12416-26. DOI
30. Zhang, L.; Dong, R.; Zhu, Z.; Wang, S. Au nanoparticles decorated ZnS hollow spheres for highly improved gas sensor performances.

- Sens. Actuators. B.: Chem.* **2017**, *245*, 112-21. DOI
31. Zhang, J.; Liu, X.; Wu, S.; Xu, M.; Guo, X.; Wang, S. Au nanoparticle-decorated porous SnO<sub>2</sub> hollow spheres: a new model for a chemical sensor. *J. Mater. Chem.* **2010**, *20*, 6453. DOI
  32. Kaskow, I.; Decyk, P.; Sobczak, I. The effect of copper and silver on the properties of Au-ZnO catalyst and its activity in glycerol oxidation. *Appl. Surf. Sci.* **2018**, *444*, 197-207. DOI
  33. Rahbarpour, S.; Sajed, S.; Ghodsi, N.; Ghafoorifard, H. Operating temperature dependence of sensitivity in Ag-TiO<sub>2</sub> Schottky type gas sensors. *Mater. Res. Express.* **2019**, *6*, 085905. DOI
  34. Hsueh, T.; Hsu, C. Fabrication of gas sensing devices with ZnO nanostructure by the low-temperature oxidation of zinc particles. *Sens. Actuators. B.: Chem.* **2008**, *131*, 572-6. DOI
  35. Zhang, J.; Ma, S.; Wang, B.; Pei, S. Hydrothermal synthesis of SnO<sub>2</sub>-CuO composite nanoparticles as a fast-response ethanol gas sensor. *J. Alloys. Compd.* **2021**, *886*, 161299. DOI
  36. Wang, J.; Li, Z.; Zhang, S.; et al. Enhanced NH<sub>3</sub> gas-sensing performance of silica modified CeO<sub>2</sub> nanostructure based sensors. *Sens. Actuators. B.: Chem.* **2018**, *255*, 862-70. DOI
  37. Young, S.; Chu, Y. Hydrothermal synthesis and improved CH<sub>3</sub>OH-sensing performance of ZnO nanorods with adsorbed Au NPs. *IEEE. Trans. Electron. Devices.* **2021**, *68*, 1886-91. DOI
  38. Wang, S.; Xiao, B.; Yang, T.; et al. Enhanced HCHO gas sensing properties by Ag-loaded sunflower-like In<sub>2</sub>O<sub>3</sub> hierarchical nanostructures. *J. Mater. Chem. A.* **2014**, *2*, 6598-604. DOI
  39. Yan, S.; Ma, S.; Li, W.; et al. Synthesis of SnO<sub>2</sub>-ZnO heterostructured nanofibers for enhanced ethanol gas-sensing performance. *Sens. Actuators. B.: Chem.* **2015**, *221*, 88-95. DOI
  40. Pei, S.; Ma, S.; Xu, X.; Almamoun, O.; Ma, Y.; Xu, X. Exploring gas-sensing characteristics of (CH<sub>2</sub>OH)<sub>2</sub> with controlling the morphology of BiVO<sub>4</sub> by adjusting pH of solution. *J. Alloys. Compd.* **2021**, *859*, 158400. DOI
  41. Mirzaei, A.; Leonardi, S.; Neri, G. Detection of hazardous volatile organic compounds (VOCs) by metal oxide nanostructures-based gas sensors: a review. *Ceram. Int.* **2016**, *42*, 15119-41. DOI
  42. Gao, Y.; Wang, X.; Zhang, Z.; et al. Synthesis of ZnO nanosheets @In<sub>2</sub>O<sub>3</sub> hollow micro-rods heterostructures for enhanced ethanol gas sensing performance. *Sens. Actuators. B.: Chem.* **2024**, *404*, 135271. DOI
  43. Wen, Z.; Tian-mo, L. Gas-sensing properties of SnO<sub>2</sub>-TiO<sub>2</sub>-based sensor for volatile organic compound gas and its sensing mechanism. *Phys. B.: Condens. Matter.* **2010**, *405*, 1345-8. DOI
  44. Pei, S.; Ma, S.; Xu, X.; Xu, X.; Almamoun, O. Modulated PrFeO<sub>3</sub> by doping Sm<sup>3+</sup> for enhanced acetone sensing properties. *J. Alloys. Compd.* **2021**, *856*, 158274. DOI
  45. Doan, T. L. H.; Kim, J.; Lee, J.; et al. Preparation of n-ZnO/p-Co<sub>3</sub>O<sub>4</sub> heterojunctions from zeolitic imidazolate frameworks (ZIF-8/ZIF-67) for sensing low ethanol concentrations. *Sens. Actuators. B.: Chem.* **2021**, *348*, 130684. DOI
  46. Qin, C.; Wang, Y.; Gong, Y.; Zhang, Z.; Cao, J. CuO-ZnO hetero-junctions decorated graphitic carbon nitride hybrid nanocomposite: hydrothermal synthesis and ethanol gas sensing application. *J. Alloys. Compd.* **2019**, *770*, 972-80. DOI
  47. Xiong, Y.; Xu, W.; Zhu, Z.; et al. ZIF-derived porous ZnO-Co<sub>3</sub>O<sub>4</sub> hollow polyhedrons heterostructure with highly enhanced ethanol detection performance. *Sens. Actuators. B.: Chem.* **2017**, *253*, 523-32. DOI
  48. Zhao, S.; Shen, Y.; Hao, F.; et al. P-n junctions based on CuO-decorated ZnO nanowires for ethanol sensing application. *Appl. Surf. Sci.* **2021**, *538*, 148140. DOI
  49. Kamalianfar, A. Promotional effects of Ag decoration on root-like ZnO microstructures for ethanol sensing. *J. Mater. Sci.: Mater. Electron.* **2023**, *34*, 10678. DOI